Accelerating Water Oxidation on $BiVO_4$ Photoanodes via Surface Modification with Co Dopants

Mahsa Barzgar Vishlaghi[1,2,†], Abdullah Kahraman[1,2], Nicklas Österbacka[3], Emre Usman[1,2,‡], Emre Erdem[4], Alphan Sennaroğlu[5,6], Julia Wiktor[3,*], Sarp Kaya[2,6,7 *]

[1] Materials Science and Engineering, Koç University, 34450 Istanbul, Türkiye

[2] Koç University Tüpraş Energy Center (KUTEM), 34450 Istanbul, Türkiye

[3] Department of Physics, Chalmers University of Technology, SE-412 96, Gothenburg, Sweden

[4] Materials Science and Nano Engineering, Sabancı University, 34956 Istanbul, Türkiye

[5] Departments of Physics and Electrical-Electronics Engineering, Koç University, Istanbul 34450, Türkiye

[6] Koç University Surface Science and Technology Center (KUYTAM), Istanbul 34450, Türkiye

[7] Department of Chemistry, Koç University, 34450 Istanbul, Türkiye

[†] Present address: Institute for Solar Fuels, Helmholtz-Zentrum Berlin für Materialien und Energie GmbH, Hahn-Meitner-Platz 1, Berlin, 14109 Germany

[‡] Present address: Department of Chemistry, University of Wisconsin-Madison, Madison, Wisconsin 53706, United States

*Corresponding authors: sarpkaya@ku.edu.tr (Sarp Kaya), julia.wiktor@chalmers.se (Julia Wiktor)

Keywords

$BiVO_4$; surface doping; trapping; atomic layer deposition; transient absorption spectroscopy.

Abstract

Despite the vast investigations on improving the photoelectrochemical performance of $BiVO_4$ for water splitting, charge recombination in the near-surface region remains a challenge. In this study, we showed that the diffusion of Co^{2+} ions into the $BiVO_4$ subsurface boosted the water oxidation activity and charge injection efficiency remarkably. The increase in the concentration of oxygen vacancies upon the incorporation of cobalt ions was shown by electron paramagnetic resonance (EPR) spectroscopy and confirmed by Density functional theory (DFT) calculations. DFT calculations revealed that vanadium sites in the subsurface region were the most favorable sites for substitution with cobalt ions. Charge localization at surface oxygen vacancies was found less favorable in the presence of cobalt in the subsurface layer, eliminating surface recombination. This resulted in 4.25 times larger charge injection efficiency and 6.2 times higher photocurrent current density at the potential of ~0.6 V, as compared to pristine $BiVO_4$. This enhancement was significantly larger as compared to CoO_x-loaded $BiVO_4$, indicating that the suppressed recombination at the surface and improved

charge transfer kinetics obtained solely by CoO_x deposition are not sufficient for enhanced activity of $BiVO_4$. A longer charge carrier lifetime obtained upon cobalt incorporation was observed by transient absorption spectroscopy and verified the reduced rate of recombination.

Introduction

Photoelectrochemical (PEC) water splitting is a promising renewable pathway to convert solar energy to chemical energy stored in hydrogen bonds [1]. The development of efficient photoanodes for water splitting has attracted a great deal of attention in recent years [2]. Monoclinic $BiVO_4$ is one of the best photoanode materials for the oxidation of water so far [2,3], with a proper bandgap for visible light absorption and a suitable valence band edge position to drive the water oxidation reaction. $BiVO_4$ is known to suffer from poor electron conductivity and short charge carrier diffusion length, which can be solved by doping electron donors into bulk and by morphology engineering [4–9]. However, a more important drawback of $BiVO_4$ which remains unsolved is facile charge recombination and poor charge transfer kinetics at the surface [9–12]. It is revealed that poor charge separation at the surface is more dominant than the slow charge transfer rate in $BiVO_4$ [11,13]. Several surface modifications have been shown to reduce surface charge recombination and increase the charge transfer kinetics [12,14]. Utilizing oxygen evolution catalysts (OEC) such as CoO_x, FeOOH, NiOOH, and NiO_x are generally shown to increase the kinetics of charge transfer at $BiVO_4$/electrolyte interface [9,15,16], whilst some OECs such as CoPi or $(Ce\text{-}Fe)O_x$ have been shown to passivate the surface defects and reduce the interfacial charge recombination rather than enhancing the charge transfer kinetics [13,17,18]. Surface defects such as oxygen vacancies (V_O) play an important role in the PEC performance of metal oxide semiconductors [19]. In $BiVO_4$, V_Os in the bulk are known to be responsible for its intrinsic n-type character [20,21], and their presence at the surface is evidenced to aggravate the PEC performance [22]. However, there are still controversies regarding the role of V_Os in $BiVO_4$. V_Os can increase the carrier density and conductivity by creating shallow donor states in the bulk [4,23], while they can act as recombination sites by forming deep trap states at the surface [24]. Selim et al. reported that the states created by V_O in the bulk can trap photogenerated holes, while electrons are trapped in the V_O in the space charge layer [25]. Other researchers showed a positive impact of V_O by increasing the active adsorption sites at the surface [26].

Although most of the doping strategies are used for solving the poor conductivity problem of $BiVO_4$ in the bulk [6,27], the changes at the surface V_O upon bulk doping are considered as a

concomitant effect on charge transport. Doping of $BiVO_4$ by various atoms such as W, Mo, N, and Co is reported to create V_Os in the bulk and surface and it is claimed that the optimum concentration of V_O at the surface increases the adsorption of water oxidation intermediates and helps charge transfer [5,28–30]. Gradient doping of $BiVO_4$ by Mo and Co is shown to increase the charge separation in the bulk and the near-surface region of $BiVO_4$ by introducing surface V_Os combined with the formation of a p-n junction [5,31].

Recently, more attention has been drawn to trap states in the surface region. Studies show that V_Os created by nitrogen treatment [32] and chemical reduction [33] suppress the electron trapping at surface states. In addition, the changes in the valency of atoms under the applied potential might affect the formation and stability of V_Os in $BiVO_4$ during the water oxidation reaction.

Herein, we showed that when Co ions are incorporated into the $BiVO_4$ surface, significant changes in the charge separation occurred compared to when they are deposited on the surface as a catalyst. Density functional theory (DFT) results showed that Co incorporation in the subsurface layer increases the V_Os at the surface while reducing the electron trapping at these defects. We utilized the electron paramagnetic resonance (EPR) technique which is very sensitive to detecting the low concentration of ionized V_Os in $BiVO_4$ [33–35], together with transient photocurrent using a short-pulsed LED and transient absorption spectroscopy (TAS) to characterize and clarify the impact of defects created by Co incorporation into the subsurface. The charge separation efficiency and the water oxidation kinetics were improved significantly. Possible mechanisms for boosting the activity are discussed.

Results and Discussion

Co incorporation (Co-$BiVO_4$) was achieved by depositing CoO_x onto the $BiVO_4$ surface ($BiVO_4$/CoO_x) by atomic layer deposition (ALD) and subsequent heat treatment. The number of ALD cycles of CoO_x was first optimized and the highest photocurrent density was obtained for photoanodes with 20 ALD cycles of CoO_x (Fig. S1). Scanning electron microscopy (SEM) images of the photoanodes presented in Fig. S2 show that the photoanodes maintained their nanoporous morphology with an average particle size of ~95 nm after the deposition of CoO_x and Co incorporation into the surface. Grazing incidence X-ray diffraction (GiXRD) patterns presented in Fig. S3 and UV-visible absorption spectra in Fig. S4 also confirm that there is no change in the extended structure (GiXRD) and optical properties (UV-vis). In Fig. S3, monoclinic $BiVO_4$ peaks were observed in both patterns. There are small peaks related to the

films with a Bi-rich core, as reported previously [36]. As the optical properties, extended crystal structures, and morphology of the photoanodes are nearly identical, the superior performance is solely associated with the changes in the near-surface region in Co-$BiVO_4$.

X-ray photoelectron spectroscopy (XPS) analysis was performed to investigate the changes at the $BiVO_4$ surface after the deposition of CoO_x and incorporation of Co into the surface. XPS spectra of Bi 4f, V 2p, and O 1s are illustrated in Fig. 1a to 1c. The analysis of bare $BiVO_4$ and $BiVO_4/CoO_x$ showed Bi $4f_{7/2}$ and Bi $4f_{5/2}$ peaks at 158.3 and 163.6 eV which implies the presence of Bi^{3+} in $BiVO_4$ [37]. V $2p_{3/2}$ and V $2p_{1/2}$ peak positions at 516.2 eV and 523.8 eV are characteristic peaks of V^{5+} in $BiVO_4$ [37,38]. Fig. 1d shows Co 2p spectra for $BiVO_4/CoO_x$ and Co-$BiVO_4$. Co 2p spectrum consists of spin-orbit split peaks at around 780.0 eV and 795.5 eV which are the characteristic peaks of Co^{2+} [39]. The decreased intensity of Co peaks in Co-$BiVO_4$ is a sign of diffusion of Co ions into $BiVO_4$. Consistent with this observation, a slight rise in the intensities of Bi 4f, V 2p, and O 1s peaks in Co-$BiVO_4$ is observed (Fig. 1a to 1c). It is reported that the incorporation of Co into $BiVO_4$ can form V_Os [40], which are coupled to V^{4+}. Angle-dependent XPS measurements were performed to confirm the diffusion of Co into subsurface layers. Table S1 shows the different Bi/Co atomic ratios at different measurement angles and corresponding Co 2p and Bi 4f XPS spectra are shown in Fig. S5. A greater ratio for Co-$BiVO_4$ points out the diffusion of Co into subsurface layers. In addition, in Co-$BiVO_4$ the Bi/Co ratio at 67° is 24% larger than that in $CoO_x/BiVO_4$ while it is only 13% larger for Co-$BiVO_4$ at 0°, supporting Co diffusing into the subsurface.

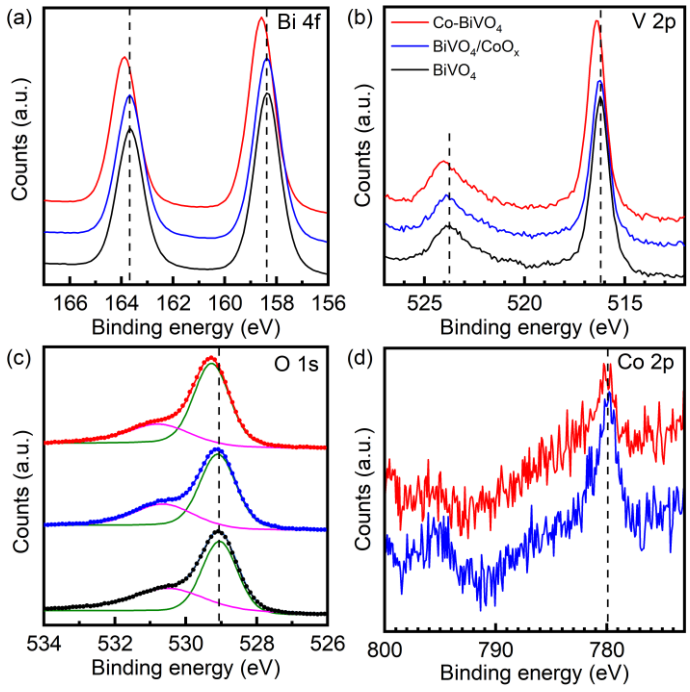


Figure 1. (a) Bi 4f, (b) V2p, (c) O1s, and (d) Co 2p XPS spectra of the films; black: $BiVO_4$, blue: $BiVO_4/CoO_x$, and red: Co-$BiVO_4$. In O 1s XPS spectra the solid lines show the deconvoluted peaks and circles represent the original data points.

The V 2p spectra of our photoanodes do not show any low binding energy shoulder related to V^{4+} and the spectra are identical for all three photoanodes. However, the absence of the V^{4+} shoulder can be due to its low concentration which is not detectable by XPS and does not neglect the presence of V_Os coupled to V^{4+} in the photoanodes. To further explore the diffusion of Co inside the $BiVO_4$ surface, we compared the binding energy positions of the substrate peaks; Bi 4f, V 2p, and O1s. According to Fig. 1a to 1c, XPS spectra show no change in the energy positions for $BiVO_4/CoO_x$ with respect to bare $BiVO_4$, while a shift of about 0.22 eV to a high binding energy side in Bi 4f, V 2p, and O 1s peaks are observed in Co-$BiVO_4$. This shift implies the change in the electronic environment of Bi and V ions by incorporation of Co ions inside the surface of $BiVO_4$ [5,41]. Jin and co-workers attributed a similar XPS shift to a change in metal cations coordination by the presence of V_Os at the surface of $BiVO_4$ [42]. We have shown in our previous work that heat treatment of bare $BiVO_4$ under similar conditions resulted in a shift of Bi 4f, V 2p, and O 1s lines to lower the binding energy side, which was ascribed to the change in Fermi-level and increased band bending at the surface [36]. The opposite shift in the XPS spectra of Bi 4f, V 2p, and O 1s in Co-$BiVO_4$ represents a change in surface Fermi-level compared to $BiVO_4/CoO_x$ and $BiVO_4$ that is a sign of different atomic arrangement due to Co diffusion into the surface. Partial reduction of the Bi, V, and O atoms due to the formation of V_Os at the surface can induce such a shift [33]. It should be noted that there is no shift in Co 2p peaks before and after heat treatment and the oxidation state of Co remains unchanged (Fig. 1d).

In the O 1s spectrum, the main peak at 529.0 eV is assigned to lattice oxygen ions, and the shoulder at about 530.8 eV is assigned to surface adsorbed species such as hydroxyl groups and dangling oxo-bonds [43]. The ratio of high binding energy shoulder to the main peaks in the O 1s spectrum is 0.91, 0.57, and 0.53 for $BiVO_4$, $BiVO_4/CoO_x$, and Co-$BiVO_4$, respectively. It can be supposed that the deposition of CoO_x in $BiVO_4/CoO_x$ using O_3 removed the surface species [44] and the heat treatment step after CoO_x deposition in Co-$BiVO_4$ further eliminated the oxygenated species from the $BiVO_4$ surface.

Fig. 2a shows the Raman spectra collected from the photoanodes. All observed peaks are related to the monoclinic $BiVO_4$ [45]. The bands at 826 cm^{-1} and 712 cm^{-1} are described as V-O

symmetric and asymmetric stretching modes, respectively. The bands around 330 cm^{-1} and 365 cm^{-1} are assigned to the bending modes of VO_4 tetrahedrons and the ones at 127 cm^{-1} and 212 cm^{-1} are related to the external modes of the lattice [45]. No change occurs after the deposition of CoO_x on $BiVO_4$ but a slight red shift is observed in Co-$BiVO_4$ for the bands at 828 cm^{-1} and 212.2 cm^{-1}. The Raman band at 828 cm^{-1} in bare $BiVO_4$ redshifts by 2 cm^{-1} in Co-$BiVO_4$ and has become asymmetric. This can be due to the formation of defects due to Co incorporation that can affect the short-range symmetry of V-O bonds in $BiVO_4$. The creation of O_Vs in the $BiVO_4$ structure causes peak broadening and peak shift in Raman spectra [23,46]. A similar redshift is reported for Co-doped $BiVO_4$ as a result of Co incorporation in the structure [8] and redshift in the Raman spectra of Mo- and W-doped $BiVO_4$ has been attributed to the incorporation of Mo and W in $BiVO_4$ [8,47].

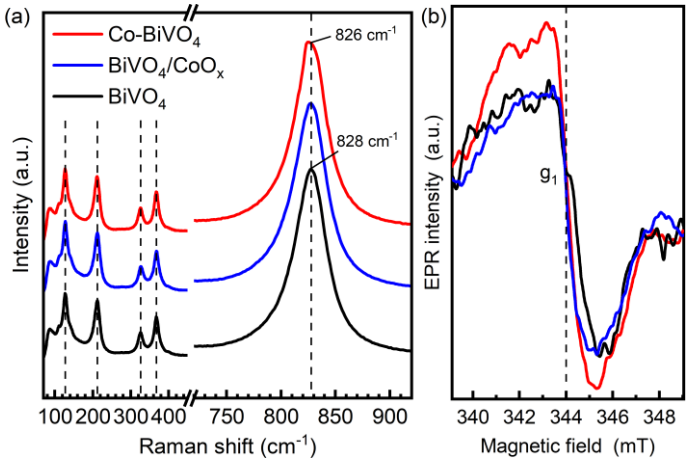


Figure 2. (a) Raman spectra and (b) EPR spectra of the photoanodes.

In order to monitor the changes in V_Os concentration in the photoanodes, we utilized EPR spectroscopy. Due to the high sensitivity of EPR, even very low concentrations of paramagnetic V^{4+} centers in $BiVO_4$ and V_Os coupled to them can be detected [35]. In Fig. 2b, a peak signal at g_1=2.0018 is detected for all three photoanodes, which is related to V^{4+} in $BiVO_4$ [34,48]. The EPR peak has more intensity in Co-$BiVO_4$ compared to $BiVO_4/CoO_x$ and $BiVO_4$, which verifies a larger concentration of V_Os in Co-$BiVO_4$. The formation of V_Os in $BiVO_4$ by Co doping is reported earlier which confirms our findings [5].

Co incorporation into $BiVO_4$ was investigated by means of DFT. The defect formation energies for the dopant as an interstitial as well as a substitutional defect on vanadium and bismuth sites in the lattice were computed. The resulting relative formation energies are shown in Fig. 3a for chemical potentials corresponding to O-poor and Bi-rich conditions that

are expected for *n*-type $BiVO_4$ according to a previous theoretical study by Österbacka *et al.* [49]. Formation energies for other chemical potentials are shown in Fig. S6. The inset numbers represent the expected oxidation state of the Co atom for each charge state the defect may take on, calculated by partitioning the electron density using maximally localized Wannier functions. The number of Wannier centers that lie closest to the dopant is counted and compared to the number of electrons required to neutralize the atom's core charge. The difference between the two quantities then gives the oxidation number.

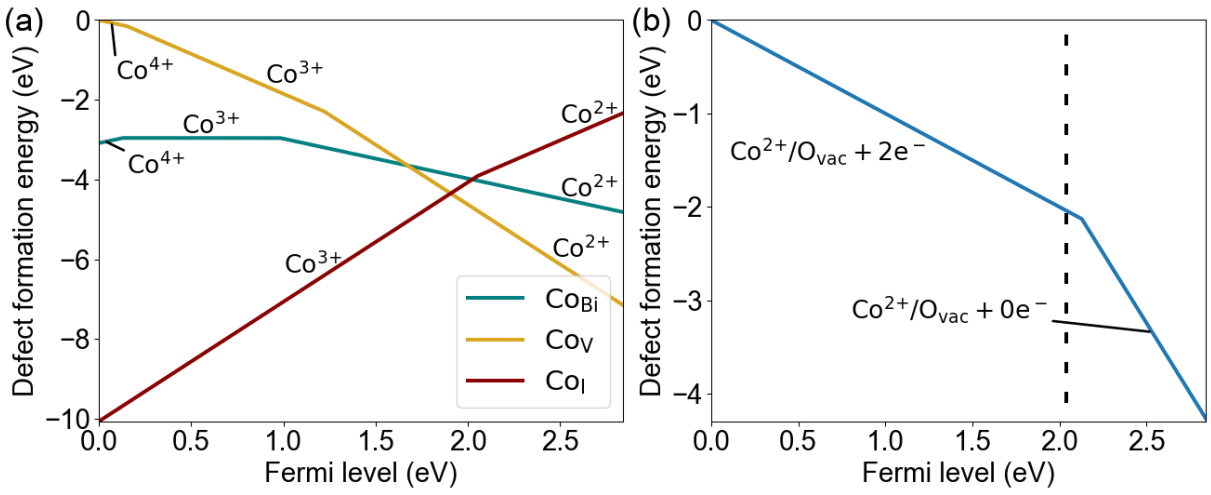


Figure 3. Defect formation energies for (a) Co insertion at Bi (green), V (yellow), and interstitial (I) (maroon) sites, and for (b) the oxygen vacancy at a Co_V site in different charge states. The numbers in (a) represent the oxidation state of the Co atom for each line segment, the dashed line in (b) represents the polaron level for an electron at the subsurface of the pristine material, and the text in (b) represents the configuration of the defect cluster for the two-line segments. Formation energies are given relative to the maximum value within the bandgap.

For *n*-type semiconductors, the Fermi level lies above the center of the bandgap, close to the conduction band. In this Fermi level region, Co incorporation is most favorable on vanadium sites, with the dopant replacing V in the subsurface as shown in Fig. 4a. In this configuration, the overall geometry of the VO_4 unit is preserved around the substitutional atom, though some distortions are present in the vicinity of the defect. The Co–O bonds become ~1.96 and ~1.98 Å for the oxygen oriented towards the surface and towards the bulk, respectively, rather than ~1.77 and ~1.68 Å as for subsurface VO_4 in the pristine $BiVO_4$. The dopant is expected to have an oxidation state of +2, and there are transition levels between the +2 and +3 as well as the +3 and +4 oxidation states within the bandgap. This implies that the dopant may act as a hole-trapping site. Due to its incorporation in the subsurface, the Co atom is unable to directly act as an active site for water splitting.

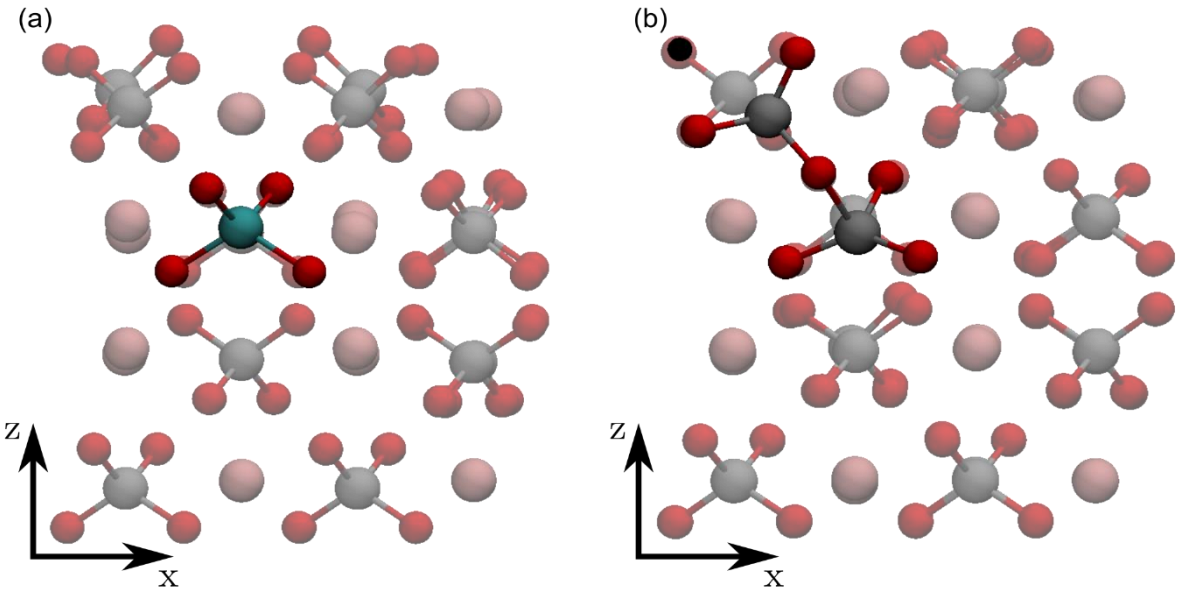


Figure 4. The atomic configurations of the (a) Co substitutional atom (green) at a V site in the subsurface and (b) an V_O at the undoped surface. Atoms surrounding the dopant and defect have been made transparent for clarity. The approximate location of the removed oxygen atom in (b) is shown in black. The surface lies in the z direction as indicated by the inset axes. Bi atoms (coral) occupy sites between VO_4 tetrahedra presented by gray (V) and red (O) atoms.

The formation of V_Os as a result of Co incorporation has been reported previously, based on charge neutrality arguments and DFT simulations [5,40]. These DFT calculations were performed only for the neutral vacancy without accounting for charge localization, and thus unable to capture the full picture of the defect. We take this phenomenon into account by means of hybrid DFT and investigate if subsurface Co doping affects the ease of removing oxygen from the lattice. In $BiVO_4$, the V_O preferentially forms in the topmost layer of the material as shown in Fig. 4b. To keep its four-fold coordination, the V atom acting as a host for the vacancy shifts towards an oxygen atom from a VO_4 in the subsurface layer, forming a V–O–V bridge [24,50]. With Co incorporated, we find that the most stable defect cluster retains this geometry, with Co replacing the subsurface V atoms. By comparing the stability of this structure with that of the vacancy being far away from the Co, we find that V_O formation involving the CoO_4 is favorable by ~300 meV. Subsurface Co incorporation on V sites is thus expected to increase the concentration of surface V_Os.

The V_O acts as an electron donor and may take on different charge states: in the neutral state, both donated electrons are present, while removing one or both results in the singly and doubly ionized +1 and +2 states, respectively. Where these excess charges localize strongly affects the stability of the defect [24,46]. At the Co-free surface, one of the two excess electrons

preferentially localizes on the bridge-forming subsurface V, while the second one localizes in the subsurface away from the defect in a fashion similar to a subsurface polaron in the pristine material. Removing one of these electrons yields a singly ionized vacancy in the +1 charge state. The remaining electron preferentially localizes on the bridge-forming V. To assess the attraction of this second electron to the V_O, we compare its stability to that of its counterpart localized further away from the defect (see Fig. S7). We find that the latter "free" electron polaron is ~230 meV less stable than the one bound to the defect. This means that while the V_O at the Co-free surface donates two electrons, only one can contribute to conductivity, while the other is strongly bound to the defect. Charge localization at the vacancy with subsurface Co present is qualitatively different, however. With both excess electrons present, one localizes on the bridge-forming V at the surface, while the other localizes in the subsurface further from the defect-dopant complex as shown in Fig. S8a. Neither of these electrons is strongly bound to the defect and they can both contribute to conductivity. The electron on the bridge-forming V at the surface is the least stable of the two and in the singly ionized case, the lone excess electron preferentially localizes on the subsurface V site far from the complex as shown in Fig. S8b. This suggests that charge localization close to V_Os is less favorable in the presence of Co in the subsurface layer. Additionally, Fig. 3b shows the defect formation energies for the Co_V-V_O complex in different charge states as a function of the Fermi level. The Co remains in the +2 oxidation throughout, and the inset numbers specify the charge state of the vacancy for each line segment: at 0, both excess electrons are present, while none of them are present at +2. The vertical line shows the polaron level for an electron in the subsurface of pristine $BiVO_4$, i.e., the Fermi level at which polaron formation occurs spontaneously. The charge transition level for electron occupancy of the dopant-defect complex lies above the polaron level; this implies that electrons preferentially form subsurface polarons far away from the Co rather than being trapped there. This behavior is different from what Wang *et al.* found for surface V_Os at the dopant-free surface, which they suggest may act as an electron trap [24].

The current-voltage behavior of the photoanodes for water oxidation is shown in Fig. 5a. Linear sweep voltammograms (LSVs) show that the photocurrent density of Co-$BiVO_4$ is significantly larger at potentials lower than 0.9 V. Enhancement of the photocurrent density at ~1.23 V is 20% for $BiVO_4/CoO_x$ and 70% for Co-$BiVO_4$ as compared to unmodified $BiVO_4$. In addition, photocurrent onsets below 0.3 V in Co-$BiVO_4$, while $BiVO_4/CoO_x$ and $BiVO_4$ have an onset at 0.6 V. Lower onset potential indicates that smaller external driving force is

required for water oxidation reaction on Co-$BiVO_4$ and higher photocurrent density at low potentials can be originated from the increased charge transfer rate at the interface of photoanode/electrolyte, or reduced recombination of the charge carriers at the photoanode surface in Co-$BiVO_4$. OECs such as CoO_x are known to increase the kinetics of the oxygen evolution reaction (OER) by increasing the charge transfer rate. However, for $BiVO_4/CoO_x$ increased photocurrent density was observed only at a higher potential (> 0.8 V), suggesting that the photocurrent at lower potentials is mainly restricted by the charge recombination in the surface region rather than the charge transfer kinetics. The presence of an oxidation peak at lower potentials in $BiVO_4/CoO_x$ and $BiVO_4$ (Fig. 5a) is attributed to the electron trapping process at surface states [28,32] and could be a sign of charge recombination. The absence of this peak in Co-$BiVO_4$ indicates that the diffusion of Co ions into the surface modifies surface states in favor of less recombination. Li and coworkers showed that TiO_2 deposited on Fe_2O_3 by ALD followed by heat treatment resulted in the diffusion of TiO_2 into the Fe_2O_3 surface and improved the defect-mediated charge transfer and increased photocurrent [51]. A study on Co-doped $BiVO_4$ suggested that a trace amount of Co^{2+} as an electron acceptor can compensate for the intrinsic defects while a large amount of dopant can increase the defects and charge recombination [5].

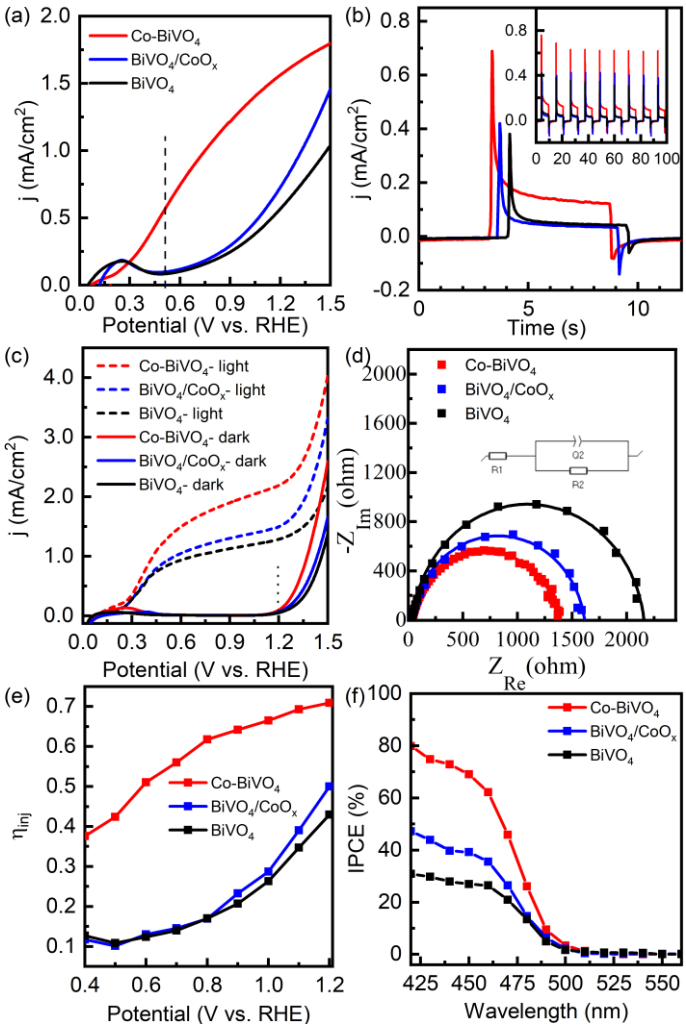


Figure 5. (a) LSV of the photoanodes. (b) Transient photocurrent behavior under chopped light at 0.5 V. Inset is the transient behavior for a longer duration (measurements are performed in 0.1 M KPi buffer with pH 7.5). (c) LSV of the photoanodes in the presence of 0.5 M Na_2SO_3 hole scavenger. (d) EIS measurement under illumination at 0.6 V. Inset shows the equivalent circuit model used for fitting EIS data. R1 is ohmic resistance in the cell, R2 is charge transfer resistance (R_{ct}) at the interface, and Q2 is the constant phase element (CPE) for the interfacial capacitance. (e) Charge injection efficiency of photoanodes. (f) IPCE measured in 0.1 M KPi buffer at 1.23 V.

Transient photocurrent (TPC) measurement under chopped light can further elucidate the effect of surface Co doping on charge accumulation and recombination. Fig. 5b shows the TPC behavior of the photoanodes at 0.5 V, which is the lowest potential at which the photocurrent raises, as shown by the dashed line in Fig. 5a. The inset in Fig. 5b shows the same measurement on a longer time scale. An anodic spike at sudden illumination appears due to the accumulation of the photogenerated electrons and holes. The larger spike in Co-$BiVO_4$ indicates that a larger amount of photogenerated electrons reach the back contact due to less charge recombination or less trapping of the electrons at defect states [52]. Considering

no significant change in the light absorption properties (Fig. S4), the observed accumulation in Co-$BiVO_4$ can only be explained by improved charge separation efficiencies near the surface region. After a quasi-exponential decay of the anodic spike, a steady state photocurrent is reached as a result of three phenomena: charge transport from bulk to the surface, recombination of these charges at the near-surface region, and charge transfer to the electrolyte at the interface [52]. Lower steady-state photocurrent in $BiVO_4/CoO_x$ and $BiVO_4$ shows facile recombination of the charges in these photoanodes. When the light is turned off, photogenerated electrons recombine with the remaining holes which are not transferred into the electrolyte, giving rise to the cathodic spike. A smaller cathodic spike in Co-$BiVO_4$ is the result of less charge remaining at the interface, while $BiVO_4/CoO_x$ and $BiVO_4$ have larger cathodic spikes due to accumulated holes that could not be transferred to the electrolyte as a consequence of slow kinetics. This observation indicates that CoO_x at the surface cannot fully suppress the recombination and increase the charge transfer kinetics. Fig. 5c shows LSV measurement in the presence of sodium sulfite (Na_2SO_3) as a hole scavenger in dark and under illumination. Easier oxidation of sulfite (SO_3^-) ions compared to water [53] allows for studying the photoanode performance without the kinetic barriers [9]. As shown in Fig. 5c, the dark onset potential shifts cathodically in $BiVO_4/CoO_x$ and further shifts in Co-$BiVO_4$. suggesting that less driving force is required for hole transfer [54]. A possibility for lower dark onset potential in Co-$BiVO_4$ can be the larger band bending in this photoanode. The impedance of the band bending can be caused by Fermi level pinning, as a result of electron traps [54,55]. We suggest that the existence of traps in pristine $BiVO_4$ and $BiVO_4/CoO_x$ is the reason for smaller band bending and consequently more anodic onset potential in dark. Flat band potentials obtained by Mott-Schottky measurement, which are discussed later, further confirm this hypothesis.

The highest photocurrent density in the presence of a hole scavenger further confirms the reduced charge recombination in Co-$BiVO_4$. We investigated the charge transfer resistance at the interface of the photoanode/electrolyte using electrochemical impedance spectroscopy (EIS). Fig. 5d shows the Nyquist plots of the photoanodes under illumination at 0.6 V in the absence of a hole scavenger. Only one semicircle in all samples is present which recommends the existence of one charge transfer mechanism at the surface; charge transfer from the photoanode to the electrolyte. The diameter of the semicircle shows the charge transfer resistance (R_{ct}) [56]. In Fig. 5d, R_{ct} of 2170, 1620, and 1399 ohms were obtained for $BiVO_4$, $BiVO_4/CoO_x$, and Co-$BiVO_4$, respectively, by EIS data fitted using Randle's model (Fig. 5d

inset) [56]. A significant decrease in the R_{ct} of $BiVO_4/CoO_x$ indicates facilitated charge transfer and the lowest R_{ct} of Co-$BiVO_4$ can be attributed to an augmented improvement in charge transfer kinetics and reduced charge recombination. Electrochemical surface area (ECSA) measurements (Fig. S9) show similar active areas for the photoanodes, ruling out any impact from the surface area difference on the activity and EIS tests. Better kinetics of the reaction in Co-$BiVO_4$ is further confirmed by Tafel plots (Fig. S10). Tafel slopes for bare $BiVO_4$, $CoO_x/BiVO_4$, and Co-$BiVO_4$, and are 988, 575, and 360 mV/dec, respectively. A lower Tafel slope indicates favorable reaction kinetics in Co-$BiVO_4$.

The charge injection efficiencies (η_{inj}) of the photoanodes shown in Fig. 5e complement the LSV results. The η_{inj} of Co-$BiVO_4$ is significantly higher than that of $BiVO_4/CoO_x$ and $BiVO_4$, which is more discernible at low potentials. η_{inj} for $BiVO_4/CoO_x$ rises after 0.8 V with respect to the bare $BiVO_4$. However, Co-$BiVO_4$ shows η_{inj} 4.25 times larger than that of $BiVO_4/CoO_x$ and $BiVO_4$ at 0.6 V. This is due to the enhanced charge separation at the surface, which results in less charge recombination and better charge injection into the electrolyte. Fig. 5f represents the incident photon conversion efficiency (IPCE) of the photoanodes in 0.1 M KPi buffer at 1.23 V. At each wavelength IPCE for Co-$BiVO_4$ is the highest. The stability of the photoanodes in 0.1 M KPi buffer at 1.23 V is shown in Fig. S11. An initial decrease of photocurrent is observed in all photoanodes, a higher photocurrent density of Co-$BiVO_4$ is however maintained.

To investigate the effect of surface Co doping on conductivity and capacitive behavior of the photoanodes, Mott-Schottky (MS) analysis was performed at 1 kHz frequency (Fig. S12). The details of the calculations can be found in the SI. The positive slope of the linear parts of MS plots is the indication of an n-type semiconductor, as expected for $BiVO_4$-based photoanodes. Rising $1/C^2$ values at different potentials for each photoanode represent their different capacitive behavior [57], due to dissimilar subsurface regions (where the space charge layer capacitance creates the Schottky barrier). The intercept of MS tangents with the potential axis shows the flat band potential (V_{fb}) of the photoanodes. V_{fb} increases in the order of Co-$BiVO_4$ < $BiVO_4/CoO_x$ < $BiVO_4$. It can be hypothesized that the larger (more positive) flat band potentials can be due to the presence of trap states in the subsurface region of these photoanodes. The trap states can pin the Fermi level at their energy states and prevent the flattening of the band under illumination [58]. DFT calculation results support this hypothesis; V_Os created near Co dopants are less likely to trap the electrons, while they can be trap centers in the absence of Co. The presence of CoO_x on the surface can also suppress the

surface charge trapping and Fermi-level pinning, which leads to a lower V_{fb} in $BiVO_4/CoO_x$ compared to that in $BiVO_4$.

The slope of the MS plot is proportional to the charge carrier density, N_d, in photoanodes [58]. N_d values calculated from the MS equation are 2.8×10^{21}, 1.9×10^{21}, and 1.5×10^{21} $1/cm^3$ for Co-$BiVO_4$, $BiVO_4/CoO_x$, and $BiVO_4$, respectively. A small increase in the N_d value of Co-$BiVO_4$ agrees with DFT results which suggested that more free electrons exist in this photoanode.

To better understand the effect of V_Os on the superior activity of Co-$BiVO_4$ and the behavior of photoanodes under light, we performed an experiment using a short-pulsed LED light and illuminated the photoanodes for 50 ms under different applied potentials (Fig. 6). LED response of the photoanodes can be divided into three sections: (i) light-on (at time zero) before reaching the steady state, (ii) steady state, (iii) light-off and the current decay. Photoanodes showed significantly different behavior in these three sections.

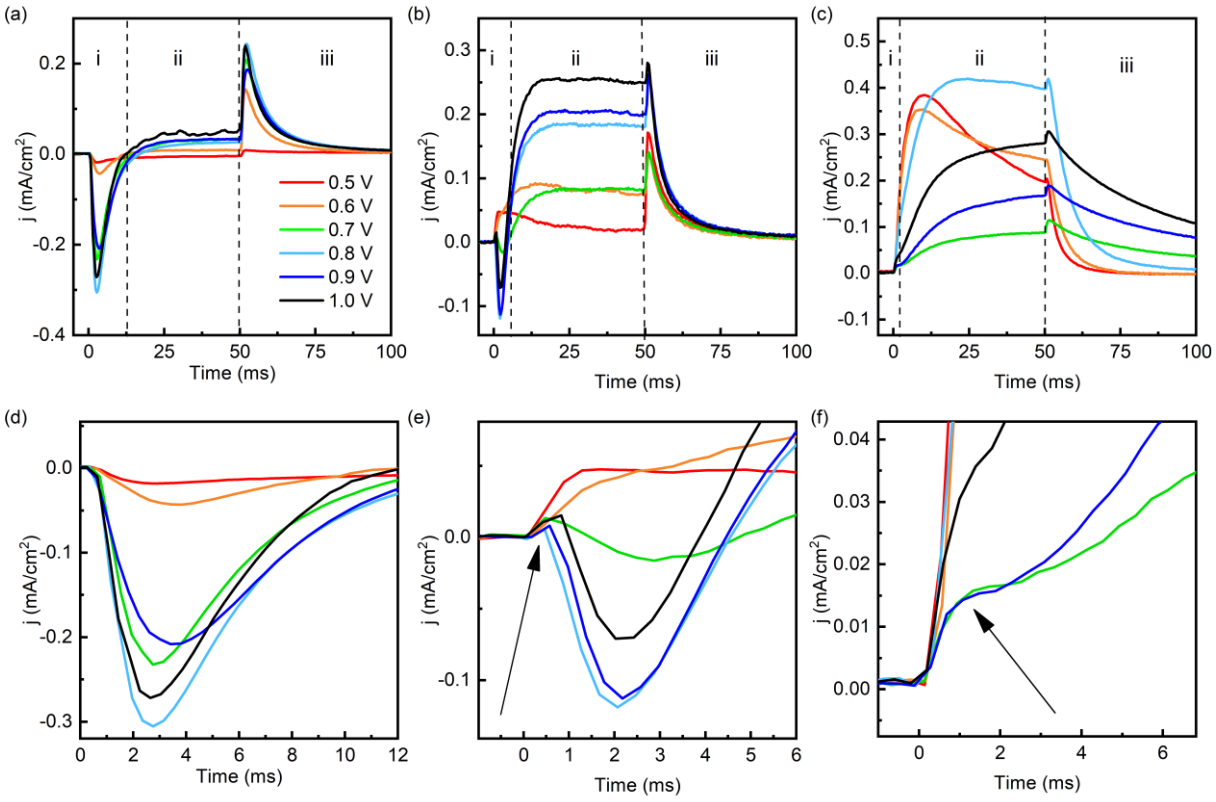


Figure 6. TPC measurement under 50 ms white LED illumination at different applied potentials in KPi buffer. (a) $BiVO_4$, (b) $BiVO_4/CoO_x$ and (c) Co-$BiVO_4$. The light-on moment of TPCs of (d) $BiVO_4$, (e) $BiVO_4/CoO_x$, and (f) Co-$BiVO_4$ in sections i of (a), (b), and (c).

$BiVO_4$: In pristine $BiVO_4$, a cathodic peak appears at V > 0.4 V when the light is on and its magnitude increases by increasing the applied potential (Fig. 6a, section i). As shown in our previous work, this peak is attributed to the trapping of photogenerated electrons in trap states near the conduction band [32,55]. The redox reaction of V^{5+}/V^{4+} ($V^{5+} + e^- \rightleftarrows V^{4+}$), which predominantly occurs between 0.6 and 0.8 V, perturbs charge separation under anodic potential and leads to the transfer of fewer electrons to the back contact, resulting in a cathodic peak. A significant increase in cathodic photocurrent is observed when the potential is increased from 0.6 V to 0.7 V (Fig. 6d) and the largest cathodic peak appears at 0.8 V, indicating maximized trapping at this potential. In section ii, the steady state current following the cathodic transient shows the Faradic current, corresponding to the hole transfer to the electrolyte. It appears after saturation of the traps while the remaining photogenerated electrons are moved to the back contact without further recombination. Very low steady-state photocurrent in $BiVO_4$ indicates that most of the electrons recombine with holes due to the presence of a large number of trap states (Fig. 5a). In section iii, an anodic peak appears when the light is turned off, due to a sudden flow of the accumulated holes to the $BiVO_4$/electrolyte interface and de-trapping of electrons. This anodic peak exists in all three photoanodes, indicating that accumulation happens in all samples, but to different extents. The decay of photocurrent following the anodic spike in section iii is due to the gradual recombination of photogenerated charges in the absence of light.

$BiVO_4/CoO_x$: In section i, the cathodic peak is present at V > 0.5 V when the light is on (Fig. 6b), and the peak area is about three times smaller than that of pristine $BiVO_4$ (Fig. 6a). This indicates a decrease in the number of traps at the surface of $BiVO_4$ by CoO_x deposition, also emphasize that trapping takes place mainly in the surface region. The higher steady-state current in section ii is an indication of more efficient hole utilization in this sample compared to pristine $BiVO_4$, which is the result of facilitated hole transport via surface CoO_x and reduced charge recombination due to decreased trapping, as indicated by a smaller cathodic peak in section i. The steady-state photocurrent is higher than that in $BiVO_4$ at all potentials because of less charge recombination and more rapid charge transfer. Another important observation in section i is a small oxidation peak at the start of the illumination which appears at $V \geq 0.7$ V, as shown by an arrow in Fig. 6e. The potential at which this peak appears coincides with the oxidation of Co^{2+} to higher oxidation states [59]. It should be noted that the steady-state photocurrent in section ii increases significantly when the applied potential increases from 0.7 to 0.8 V (Fig. 6b). A simultaneous increase in the photocurrent and

appearance of Co oxidation peak at 0.8 V suggests that the water oxidation reaction occurs through the Co^{3+} ions at the surface. The coincidence of maximized electron trapping at 0.8 V (light blue peak in Fig. 6e) and the photocurrent jump at this potential imply that the hole transfer via Co ions at the surface overcomes the recombination at trap states. Photocurrent and η_{inj} kick off at 0.8 V (Fig. 5a and 5e) confirm the suggested hypothesis. Therefore, it can be proposed that CoO_x at the surface improves the water oxidation by two mechanisms; suppressing the surface recombination by eliminating the electron traps and catalyzing the water oxidation reaction through Co ions. It is worth mentioning that oxidation of Co ions can occur via two different pathways: electrochemical oxidation under the applied potential ($Co^{2+} \rightarrow Co^{3+} + e^-$), and photo-oxidation by the holes coming from the valence band of $BiVO_4$ under illumination ($Co^{2+} + h^+ \rightarrow Co^{3+}$). Co ions can be oxidized through both pathways under the reaction conditions.

Co can have an oxidation state of 3+ in CoOOH or it can be oxidized to a 4+ state in KPi during water oxidation [60]. Although we cannot certainly define which one is formed during the reaction, this does not change the assumptions for the water oxidation mechanism through Co ions in our photoanodes. The anodic peak intensity at the light-off moment is much smaller in $BiVO_4/CoO_x$ compared to pristine $BiVO_4$, designating the decreased concentration of trapped electrons. This further confirms the better charge transfer and water oxidation kinetics due to the presence of Co ions at the surface.

Co-$BiVO_4$: In Co-$BiVO_4$, the photocurrent transient behavior at all three sections is different from the two other electrodes. There is no cathodic peak in section i (Fig. 6c and 6f), indicating the absence of electron trapping. As shown by DFT calculations, electron localization is unlikely at surface V_Os created by Co_V, therefore, Co doping has eliminated the electron trapping. However, dopant clusters are shown to be hole-trapping sites deep in the band gap. In section ii, decreasing photocurrent at 0.5 and 0.6 V (Fig. 6c red and orange lines) can be explained by the recombination of charges due to hole-trapping. A small oxidation peak at the start of illumination is observed at potentials higher than 0.7 V (shown by an arrow in Fig. 6f), correlated with Co oxidation, similar to $BiVO_4/CoO_x$. New V_O at the surface created by Co_V can provide favorable states for hole transfer to the electrolyte without recombination. Photocurrent decreased at 0.7 V (section ii of Fig. 6c) due to the same hole-trapping phenomena, but it increased at 0.8 V. The reason for the significant rise at 0.8 V can be explained by modifying the hole traps under applied potential. DFT results suggested that the dopant can be oxidized from 2+ to 3+ or from 3+ to 4+ by trapping photogenerated holes.

However, applied potential can also oxidize the Co sites and saturate the traps. This can lead to the transfer of photogenerated holes to the surface and proceed with the water oxidation reaction. Therefore, maximum photocurrent is observed at a steady state in Co-$BiVO_4$. We propose that the oxidized Co_V at this potential acts as a mediator for photogenerated holes; transferring them to the surface V_O sites.

When the light is turned off there is another noticeable difference in the current decay behavior (section iii in Fig 6c). The slower decay of the photocurrent at V > 0.7 V is significant, indicating that accumulated charges do not recombine immediately in the absence of light. This can suggest that trapped holes at Co_V clusters that are spread deeper in the bandgap recombine with the electrons and it takes a longer time compared to the direct recombination of electrons with valence band holes. The longer lifetime of the charge carriers in Co-$BiVO_4$ is corroborated by TAS measurements shown in Fig. 7.

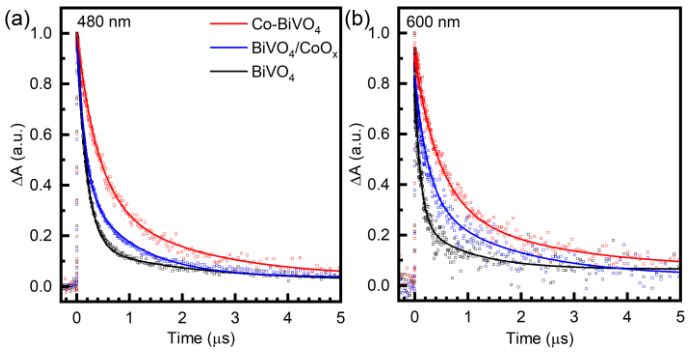


Figure 7. (a) Transient absorption decay kinetic traces of $BiVO_4$ (black), $BiVO_4/CoO_x$ (blue), and Co-$BiVO_4$ (red) probed at 480 nm and (b) 600 nm. Empty squares are the data points, solid lines are exponential decay fits. All kinetics are normalized to the maximum. The pump fluence and wavelength are 530 μj/cm^2 and 320 nm, respectively.

The carrier lifetime of semiconductors can be longer than microseconds at the surface [61] and the effect of the surface modification on the carrier lifetime can be observed by time-resolved spectroscopy. Fig. 7 shows the transient absorption kinetics at 480 nm and 600 nm which were assigned predominantly to photogenerated electron and hole carriers, respectively [10]. As also shown in Table S2, the carrier lifetime in $BiVO_4/CoO_x$ is longer than that in pristine $BiVO_4$. Since CoO_x is atomically thin, the enhanced η_{inj} most likely originated from suppression of the surface recombination, corroborating the η_{inj} results (Fig. 5e). Further enhanced carrier lifetime for Co-$BiVO_4$ supports the idea that Co incorporation into the surface suppresses further the recombination of charges due to the facilitated hole transfer to the electrolyte. Slower decay in transient photocurrents at the light-off moment in Co-$BiVO_4$

(Fig. 6c) is in good agreement with the longer carrier lifetime in this photoanode. Less number of traps in Co-$BiVO_4$ along with the faster kinetics of the hole transfer to the electrolyte through the surface Co ions delays the recombination and results in a longer lifetime of the charge carriers.

We have shown the possible pathways for water oxidation in our three photoanodes schematically in Fig. 8. The results of our work demonstrate how changing the surface region of $BiVO_4$ during the reaction can affect the charge transfer and PEC performance of the photoanodes. Charge recombination at V^{5+} traps occurs in $BiVO_4$ due to V^{5+} species present in this sample. Deposition of CoO_x decreases the surface recombination process by passivation of the surface trap states. Therefore, charge recombination is less in $BiVO_4/CoO_x$ compared to $BiVO_4$. Co-$BiVO_4$ further decreased the charge trap centers and recombination at the centers is negligible compared to the two other photoanodes. Hole transfer can occur through the valence band more efficiently in Co-$BiVO_4$ while there is less charge trapping and recombination.

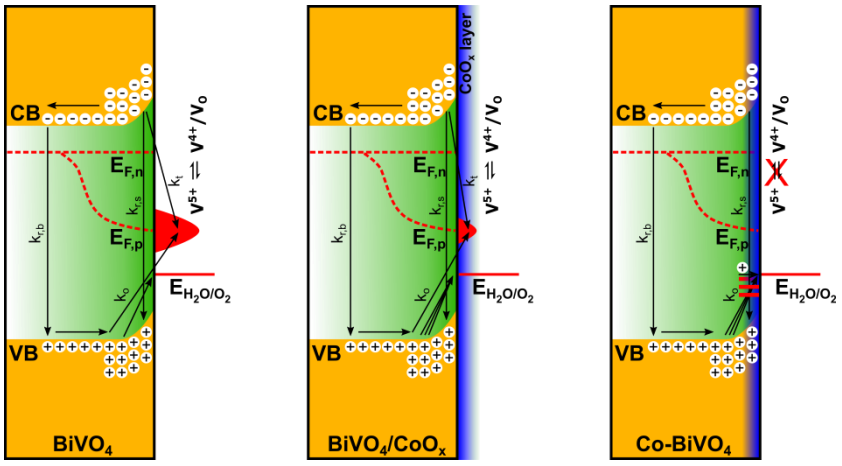


Figure 8. Schematic representation of charge transfer and recombination mechanisms in our photoanodes. CB: conduction band, VB: valence band, $E_{F,n}$: quasi-Fermi level for electrons, $E_{F,p}$: quasi-Fermi level for holes, $k_{r,b}$: bulk recombination rate constant, $k_{r,s}$: surface recombination rate constant, k_t: electron trapping rate constant, and k_o: oxidation rate constant.

Conclusions

The diffusion of Co ions into the subsurface region of nanoporous $BiVO_4$ boosted its water oxidation activity and charge injection efficiency significantly. EPR results showed that the incorporation of Co ions into the $BiVO_4$ surface region increased the concentration of V_Os which were electron traps and recombination sites. DFT results corroborated EPR results,

indicating that Co substitutes V in the subsurface layer and creates a V_O at the surface which is not likely to trap electrons. A remarkably larger increase in η_{inj} and photocurrent density was obtained when Co ions were incorporated into the surface, indicating the more dominant role of charge recombination near the surface region compared to sluggish charge transfer kinetics. Once incorporated in the subsurface region, Co ions do not contribute directly to the water oxidation, but eliminate the surface electron traps and lead to better charge transfer. The charge carrier lifetime was longer when Co was incorporated into the surface, verifying the reduced recombination. The results of this work elucidated how the incorporation of a lower valency state ion like Co^{2+} in the subsurface region modified the trap states in favor of better charge separation in nanoporous $BiVO_4$.

Acknowledgments

The authors would like to thank The Scientific and Technical Research Council of Turkey (TUBITAK) for support (Grant number: 221Z070). The authors thank KUYTAM for the characterization measurements. N.O. and J.W. acknowledge funding from "Genie" and "Area of Advance - Materials Science" at Chalmers University of Technology, and the Swedish Research Council (2019-03993). The computations were performed on resources provided by the Swedish National Infrastructure for Computing (SNIC) at NSC, C3SE, and PDC.

Conflict of Interest

The authors declare no conflict of interest.

Author Contributions

The author's contribution is as follows: Conceptualization (M.B.V., S.K., N.O., and J.W.); Data Curation, Investigation, and Methodology (M.B.V., A.K., N.O., and E.U.); Funding Acquisition and Supervision (S.K., A.S., and J.W.); Resources (S.K., A.S., E.E, and J.W.); Writing—Original Draft (M.B.V. and N.O.); Writing—Review and Editing (M.B.V., A.K., N.O., E.U., A.S., E.E, J.W., and S.K.).

References

1 M. G. Walter, E. L. Warren, J. R. McKone, S. W. Boettcher, Q. Mi, E. A. Santori and N. S. Lewis, *Chem. Rev.*, 2010, **110**, 6446–6473.
2 Z. Wang, C. Li and K. Domen, *Chem. Soc. Rev.*, 2019, **48**, 2109–2125.
3 J. H. Kim and J. S. Lee, *Adv. Mater.*, 2019, **31**, 1806938.
4 W.-J. Yin, S.-H. Wei, M. M. Al-Jassim, J. Turner and Y. Yan, *Phys. Rev. B*, 2011, **83**, 155102.

5 B. Zhang, H. Zhang, Z. Wang, X. Zhang, X. Qin, Y. Dai, Y. Liu, P. Wang, Y. Li and B. Huang, *Applied Catalysis B: Environmental*, 2017, **211**, 258–265.
6 V. Nair, C. L. Perkins, Q. Lin and M. Law, *Energy & Environmental Science*, 2016, **9**, 1412–1429.
7 F. F. Abdi, T. J. Savenije, M. M. May, B. Dam and R. van de Krol, *J. Phys. Chem. Lett.*, 2013, **4**, 2752–2757.
8 B. Zhou, X. Zhao, H. Liu, J. Qu and C. P. Huang, *Applied Catalysis B: Environmental*, 2010, **99**, 214–221.
9 T. W. Kim and K.-S. Choi, *Science*, 2014, **343**, 990–994.
10 A. Kahraman, M. Barzgar Vishlaghi, I. Baylam, A. Sennaroglu and S. Kaya, *J. Phys. Chem. C*, 2019, **123**, 28576–28583.
11 C. Zachäus, F. F. Abdi, L. M. Peter and R. van de Krol, *Chemical Science*, 2017, **8**, 3712–3719.
12 M. Tayebi and B.-K. Lee, *Renewable and Sustainable Energy Reviews*, 2019, **111**, 332–343.
13 D. K. Zhong, S. Choi and D. R. Gamelin, *J. Am. Chem. Soc.*, 2011, **133**, 18370–18377.
14 G. Ke, F. Duan, B. Liu, X. Liu, J. Wen, B. Jia, X. Liu, H. He and Y. Zhou, *Journal of Alloys and Compounds*, 2023, **934**, 167883.
15 M. Zhong, T. Hisatomi, Y. Kuang, J. Zhao, M. Liu, A. Iwase, Q. Jia, H. Nishiyama, T. Minegishi, M. Nakabayashi, N. Shibata, R. Niishiro, C. Katayama, H. Shibano, M. Katayama, A. Kudo, T. Yamada and K. Domen, *J. Am. Chem. Soc.*, 2015, **137**, 5053–5060.
16 Y. Liu, Y. Guo, L. T. Schelhas, M. Li and J. W. Ager, *J. Phys. Chem. C*, 2016, **120**, 23449–23457.
17 Y. Liang and J. Messinger, *Phys. Chem. Chem. Phys.*, 2014, **16**, 12014–12020.
18 X. Yang, C. Du, R. Liu, J. Xie and D. Wang, *Journal of Catalysis*, 2013, **304**, 86–91.
19 G. Pacchioni, *ChemPhysChem*, 2003, **4**, 1041–1047.
20 Z. Zhao, Z. Li and Z. Zou, *Phys. Chem. Chem. Phys.*, 2011, **13**, 4746.
21 J. K. Cooper, S. Gul, F. M. Toma, L. Chen, P.-A. Glans, J. Guo, J. W. Ager, J. Yano and I. D. Sharp, *Chem. Mater.*, 2014, **26**, 5365–5373.
22 M. D. Rossell, P. Agrawal, A. Borgschulte, C. Hébert, D. Passerone and R. Erni, *Chem. Mater.*, 2015, **27**, 3593–3600.
23 G. Wang, Y. Ling, X. Lu, F. Qian, Y. Tong, J. Z. Zhang, V. Lordi, C. Rocha Leao and Y. Li, *J. Phys. Chem. C*, 2013, **117**, 10957–10964.
24 W. Wang, P. J. Strohbeen, D. Lee, C. Zhou, J. K. Kawasaki, K.-S. Choi, M. Liu and G. Galli, *Chem. Mater.*, 2020, **32**, 2899–2909.
25 S. Selim, E. Pastor, M. García-Tecedor, M. R. Morris, L. Francàs, M. Sachs, B. Moss, S. Corby, C. A. Mesa, S. Gimenez, A. Kafizas, A. A. Bakulin and J. R. Durrant, *J. Am. Chem. Soc.*, 2019, **141**, 18791–18798.
26 J. Hu, X. Zhao, W. Chen, H. Su and Z. Chen, *J. Phys. Chem. C*, 2017, **121**, 18702–18709.
27 B. Liu, X. Yan, H. Yan, Y. Yao, Y. Cai, J. Wei, S. Chen, X. Xu and L. Li, *Materials*, 2017, **10**, 976.
28 Q. Shi, S. Murcia-López, P. Tang, C. Flox, J. R. Morante, Z. Bian, H. Wang and T. Andreu, *ACS Catal.*, 2018, **8**, 3331–3342.
29 X. Zhao, J. Hu, X. Yao, S. Chen and Z. Chen, *ACS Appl. Energy Mater.*, 2018, **1**, 3410–3419.
30 T. W. Kim, Y. Ping, G. A. Galli and K.-S. Choi, *Nature Communications*, 2015, **6**, 8769.
31 F. F. Abdi, L. Han, A. H. M. Smets, M. Zeman, B. Dam and R. van de Krol, *Nat Commun*, 2013, **4**, 2195.
32 A. Kahraman, M. B. Vishlaghi, I. Baylam, H. Ogasawara, A. Sennaroğlu and S. Kaya, *J. Phys. Chem. Lett.*, 2020, **11**, 8758–8764.
33 Y. Peng, H. Wu, M. Yuan, F.-F. Li, X. Zou, Y. H. Ng and H.-Y. Hsu, *Sustainable Energy Fuels*, 2021, **5**, 2284–2293.
34 S. Wang, T. He, P. Chen, A. Du, K. (Ken) Ostrikov, W. Huang and L. Wang, *Advanced Materials*, 2020, **32**, 2001385.
35 R. Venkatesan, S. Velumani, M. Tabellout, N. Errien and A. Kassiba, *Journal of Physics and Chemistry of Solids*, 2013, **74**, 1695–1702.
36 M. Barzgar Vishlaghi, A. Kahraman and S. Kaya, *J. Phys. Chem. C*, 2020, **124**, 1337–1345.
37 L. Chen, E. Alarcón-Lladó, M. Hettick, I. D. Sharp, Y. Lin, A. Javey and J. W. Ager, *J. Phys. Chem. C*, 2013, **117**, 21635–21642.
38 G. Silversmit, D. Depla, H. Poelman, G. B. Marin and R. De Gryse, *Journal of Electron Spectroscopy and Related Phenomena*, 2004, **135**, 167–175.
39 M. C. Biesinger, B. P. Payne, A. P. Grosvenor, L. W. M. Lau, A. R. Gerson and R. St. C. Smart, *Applied Surface Science*, 2011, **257**, 2717–2730.
40 G. Liu, F. Li, Y. Zhu, J. Li and L. Sun, *RSC Advances*, 2020, **10**, 28523–28526.
41 T. D. Nguyen, Q. T. P. Bui, T. B. Le, T. M. Altahtamouni, K. B. Vu, D.-V. N. Vo, N. T. H. Le, T. D. Luu, S. S. Hong and K. T. Lim, *RSC Adv.*, 2019, **9**, 23526–23534.
42 S. Jin, X. Ma, J. Pan, C. Zhu, S. E. Saji, J. Hu, X. Xu, L. Sun and Z. Yin, *Applied Catalysis B: Environmental*, 2021, **281**, 119477.
43 J.-C. Dupin, D. Gonbeau, P. Vinatier and A. Levasseur, *Phys. Chem. Chem. Phys.*, 2000, **2**, 1319–1324.

44 M. Barzgar Vishlaghi, A. Kahraman, S. Apaydin, E. Usman, D. Aksoy, T. Balkan, S. Munir, M. Harfouche, H. Ogasawara and S. Kaya, *Electrochimica Acta*, 2021, **366**, 137467.
45 R. L. Frost, D. A. Henry, M. L. Weier and W. Martens, *J. Raman Spectrosc.*, 2006, **37**, 722–732.
46 N. Österbacka and J. Wiktor, *J. Phys. Chem. C*, 2021, **125**, 1200–1207.
47 A. J. E. Rettie, H. C. Lee, L. G. Marshall, J.-F. Lin, C. Capan, J. Lindemuth, J. S. McCloy, J. Zhou, A. J. Bard and C. B. Mullins, *J. Am. Chem. Soc.*, 2013, **135**, 11389–11396.
48 H. L. Tan, A. Suyanto, A. T. D. Denko, W. H. Saputera, R. Amal, F. E. Osterloh and Y. H. Ng, *Particle & Particle Systems Characterization*, 2017, **34**, 1600290.
49 N. Österbacka, F. Ambrosio and J. Wiktor, *J. Phys. Chem. C*, 2022, **126**, 2960–2970.
50 F. S. Hegner, D. Forrer, J. R. Galán-Mascarós, N. López and A. Selloni, *J. Phys. Chem. Lett.*, 2019, **10**, 6672–6678.
51 X. Li, P. S. Bassi, P. P. Boix, Y. Fang and L. H. Wong, *ACS Applied Materials & Interfaces*, 2015, **7**, 16960–16966.
52 L. M. Peter, *J Solid State Electrochem*, 2013, **17**, 315–326.
53 P. M. Wilkinson, B. Doldersum, P. H. M. R. Cramers and L. L. Van Dierendonck, *Chemical Engineering Science*, 1993, **48**, 933–941.
54 M. X. Tan, P. E. Laibinis, S. T. Nguyen, J. M. Kesselman, C. E. Stanton and N. S. Lewis, in *Progress in Inorganic Chemistry*, ed. K. D. Karlin, John Wiley & Sons, Inc., Hoboken, NJ, USA, 2007, pp. 21–144.
55 E. Usman, M. Barzgar Vishlaghi, A. Kahraman, N. Solati and S. Kaya, *ACS Appl. Mater. Interfaces*, 2021, **13**, 60602–60611.
56 A. Lasia, *Electrochemical impedance spectroscopy and its applications*, Springer, New York, 2014.
57 A. Adán-Más, T. M. Silva, L. Guerlou-Demourgues and M. F. Montemor, *Electrochimica Acta*, 2018, **289**, 47–55.
58 R. van de Krol and M. Grätzel, Eds., *Photoelectrochemical hydrogen production*, Springer, New York, 2012.
59 J. B. Gerken, J. G. McAlpin, J. Y. C. Chen, M. L. Rigsby, W. H. Casey, R. D. Britt and S. S. Stahl, *J. Am. Chem. Soc.*, 2011, **133**, 14431–14442.
60 J. G. McAlpin, Y. Surendranath, M. Dincă, T. A. Stich, S. A. Stoian, W. H. Casey, D. G. Nocera and R. D. Britt, *J. Am. Chem. Soc.*, 2010, **132**, 6882–6883.
61 R. Godin, A. Kafizas and J. R. Durrant, *Current Opinion in Electrochemistry*, 2017, **2**, 136–143.